Cardiovascular Research (2016) **110**, 443–454
doi:10.1093/cvr/cvw073

# Patient-derived models link re-entrant driver localization in atrial fibrillation to fibrosis spatial pattern

**Sohail Zahid[1†], Hubert Cochet[2,3†], Patrick M. Boyle[1†], Erica L. Schwarz[1], Kaitlyn N. Whyte[1], Edward J. Vigmond[2], Rémi Dubois[2], Mélèze Hocini[2,3], Michel Haïssaguerre[2,3], Pierre Jaïs[2,3], and Natalia A. Trayanova[1,4*]**

[1]Institute for Computational Medicine, Department of Biomedical Engineering, Johns Hopkins University, Baltimore, MD, USA; [2]IHU LIRYC, Electrophysiology and Heart Modeling Institute, INSERM U1045, Bordeaux, France; [3]Hôpital Cardiologique du Haut-Lévêque, CHU Bordeaux, Université de Bordeaux, Bordeaux, France; and [4]Department of Medicine, Johns Hopkins University School of Medicine, Baltimore, MD, USA

*Received 19 October 2015; revised 29 March 2016; accepted 31 March 2016; online publish-ahead-of-print 7 April 2016*

**Time for primary review: 26 days**

**Aims** The mechanisms underlying persistent atrial fibrillation (AF) in patients with atrial fibrosis are poorly understood. The goal of this study was to use patient-derived atrial models to test the hypothesis that AF re-entrant drivers (RDs) persist only in regions with specific fibrosis patterns.

**Methods and results** Twenty patients with persistent AF (PsAF) underwent late gadolinium-enhanced MRI to detect the presence of atrial fibrosis. Segmented images were used to construct personalized 3D models of the fibrotic atria with biophysically realistic atrial electrophysiology. In each model, rapid pacing was applied to induce AF. AF dynamics were analysed and RDs were identified using phase mapping. Fibrosis patterns in RD regions were characterized by computing maps of fibrosis density (FD) and entropy (FE). AF was inducible in 13/20 models and perpetuated by few RDs ($2.7 \pm 1.5$) that were spatially confined (trajectory of phase singularities: $7.6 \pm 2.3$ mm). Compared with the remaining atrial tissue, regions where RDs persisted had higher FE (IQR: 0.42–0.60 vs. 0.00–0.40, $P < 0.05$) and FD (IQR: 0.59–0.77 vs. 0.00–0.33, $P < 0.05$). Machine learning classified RD and non-RD regions based on FD and FE and identified a subset of fibrotic boundary zones present in $13.8 \pm 4.9\%$ of atrial tissue where $83.5 \pm 2.4\%$ of all RD phase singularities were located.

**Conclusion** Patient-derived models demonstrate that AF in fibrotic substrates is perpetuated by RDs persisting in fibrosis boundary zones characterized by specific regional fibrosis metrics (high FE and FD). These results provide new insights into the mechanisms that sustain PsAF and could pave the way for personalized, MRI-based management of PsAF.

**Keywords** Patient-derived atrial models • Re-entrant drivers • Computational modelling • Fibrosis • Persistent atrial fibrillation

## 1. Introduction

Atrial fibrillation (AF) is the most common cardiac arrhythmia and a major contributor to mortality and morbidity, affecting 1–2% of the worldwide population.[1] Over the past decade, catheter ablation has emerged as a potential approach to treat AF; however, the efficacy of this procedure remains limited, with a particularly low success rate (~50%) in patients with persistent AF (PsAF).[2] Treatment of this disease is further encumbered by its progressive nature—each year, at least 5% of patients with less severe forms of AF develop PsAF.[3]

Evidence from recent clinical and experimental studies suggests that PsAF might be maintained by re-entrant drivers (RDs) (i.e. rotors), but the mechanisms linking RD formation and PsAF perpetuation remain unknown.[4–6] A large number of patients with PsAF have extensive atrial structural remodelling, especially fibrosis,[7–9] which can lead to slow propagation, reduced excitability and unidirectional block[10,11] and thus to the establishment of an arrhythmogenic atrial substrate and

* Corresponding author. Tel: +1 410 516 4375; fax: +1 410 516 5294, E-mail: ntrayanova@jhu.edu

† Equal contribution first co-authors.

increased likelihood of RD formation.[12–15] Since spatial patterns of atrial fibrosis are complex and vary widely between individuals,[8,9] the precise mechanistic link between fibrotic remodelling and RDs in patients with PsAF remains elusive. Better understanding of this relationship will increase the understanding of PsAF pathophysiology and help pave the way towards personalized anti-arrhythmia treatment planning.

This study used a personalized computer simulation approach based on atrial fibrosis characterization to test the hypothesis that AF induced by programmed electrical stimulation in the fibrotic substrate is perpetuated by RDs persisting in regions with specific fibrosis spatial pattern. To achieve this goal, we developed 20 patient-derived three-dimensional (3D) atrial models that incorporated individualized representations of fibrosis derived from late gadolinium-enhanced MRI (LGE-MRI) scans. Simulations of programmed electrical stimulation were then used to determine how the locations where the organizing centres of RDs (i.e. phase singularities; RD-PSs) persist relate quantitatively to the fibrosis spatial patterns. The study thus provides a unique insight into the potential role of the fibrotic substrate in PsAF dynamics.

# 2. Methods

## 2.1 Patient population

From June 2013 to October 2014, 20 patients who had PsAF (uninterrupted AF lasting longer than 7 days) were enrolled in this study. Patients who had contraindications to MRI, history of prior catheter ablation or atrial surgery, or intra-cardiac thrombi observed during transoesophageal echocardiography were excluded. This study was approved by the Institutional Ethics Committee at the University of Bordeaux, and all patients gave informed consent. This investigation conformed to the principles outlined in the Declaration of Helsinki.

## 2.2 Reconstruction of 3D patient-derived atrial models from LGE-MRI

Cardiac magnetic resonance was performed on a 1.5T scanner (Magnetom Avanto, Siemens Medical Systems, Erlangen, Germany) equipped with a 32 channel cardiac coil. LGE-MRI was performed 15 min after the administration of gadolinium chelates using a 3D, ECG-gated, respiratory-navigated and inversion recovery-prepared Turbo Fast Low Angle Shot sequence with fat saturation (voxel size: $1.25 \times 1.25 \times 2.5$ mm$^3$).[8] In the resulting images, the biatrial wall was manually contoured, and LGE and non-LGE regions were segmented using an adaptive histogram thresholding algorithm as described previously,[16] implemented in MUSIC software (LIRYC Institute, University of Bordeaux, Inria Sophia-Antipolis, France). Details of LGE Segmentation are provided in Supplementary material online. LGE segmentation was blinded to clinical characteristics and results from computer simulations. The fibrosis burden derived from LGE segmentation was expressed as a percentage of the atrial wall. Left atrial (LA) fibrosis burden was categorized according to Utah staging, as described previously.[7] Segmented images were up-sampled to an isotropic voxel size of 400 $\mu$m$^3$ using shape-based interpolation,[17] and 3D finite element meshes were generated from the resulting high-resolution datasets using a previously developed approach.[18] In each patient-derived model, myocardial fibre orientations were assigned using a rule-based method.[19] A detailed description of the geometrical model construction methodology can be found in prior publications.[20–22] Image processing and model generation are illustrated in *Figure 1*. Details on mesh characteristics are provided in Supplementary material online, *Table S1*. The patient-derived atrial models are a powerful tool to not only dissect the underlying dynamics of AF, but could also be used to explore sinus rhythm activation in these patients, which might be difficult to accomplish in the clinic if a patient is permanently in AF.

## 2.3 Modelling of atrial electrophysiology in fibrotic and non-fibrotic regions

Myocyte membrane kinetics in non-fibrotic regions were represented with a human atrial action potential model under chronic AF conditions[23] modified[24] to fit clinical monophasic action potential recordings in patients with AF (*Figure 1C*, grey), resulting in action potential duration (APD) shorter than that of normal atrial myocytes (*Figure 1C*, dashed); further model detail is provided in Supplementary material online. At the tissue level, conductivity values were assigned so that an effective longitudinal conduction velocity of 43.39 cm/s was achieved in the non-fibrotic myocardium, which was within the range of values recorded in patients with AF.[25]

Fibrotic regions were represented with remodelled electrophysiology, anisotropy, and conduction properties. The non-fibrotic chronic AF action potential model described above was further modified as follows to represent the regional electrophysiological changes due to fibrotic remodelling[26–28]: 50% reduction in inward rectifier potassium current [$I_{K1}$]; 50% reduction in L-type calcium current [$I_{CaL}$]; and 40% reduction in sodium current [$I_{Na}$]. These ionic current modifications were consistent with changes in atrial myocytes subjected to elevated TGF-β1, a key component of the fibrogenic signalling pathway.[29,30] The resulting changes to the action potential (+15.4% APD; −7.18% resting transmembrane voltage [$V_m$]; −49.6% upstroke velocity) were consistent with those documented in fibrotic myocardium *in vitro*[31] (*Figure 1C*, green). Conductivity values in fibrotic regions were reduced by 30% to represent decreased intercellular coupling due to replacement fibrosis, collagen deposition (interstitial fibrosis), and gap junction remodelling.[12,13] Since fibrosis results in greater conduction velocity impairment in the direction transverse to cardiac fibres, the conductivity values were further modified to achieve a longitudinal transverse anisotropy ratio of 8:1.[12,13] All relevant cell- and tissue-scale model parameters are provided in Supplementary material online, *Table S1*.

## 2.4 Simulation protocol

Electrical wave propagation was governed by the monodomain formulation, and finite-element simulations were executed with the CARP software package (Johns Hopkins University and University of Bordeaux); numerical detail can be found in previous publications.[32,33] In each patient-derived model, 30 pacing sites were distributed uniformly throughout the atria (*Figure 2A*). At each pacing site, a clinically relevant programmed electrical stimulation pacing sequence[34] of 14 stimulation pulses with cycle lengths decreasing from 300 to 150 ms in 25 ms intervals was applied to induce AF and assess the arrhythmogenic propensity of the fibrotic substrate. For each of the 20 patient-derived models, we simulated 30 AF induction protocols (1 for each pacing site). A patient model was categorized as inducible for AF if at least 2.5 s of self-sustained AF was observed after the last pacing stimulus.

## 2.5 Analysis of arrhythmia dynamics and identification of re-entrant drivers in simulations

Phase singularities were identified throughout the patient atrial models via phase-space analysis during a 1 s interval of AF; this involved converting transmembrane potential ($V_m$) maps into action potential phase maps and identifying points around which the line integral of the phase was equal to $\pm 2\pi$.[35] An unsupervised density-based spatial clustering algorithm[36] was then used to spatiotemporally cluster all phase singularities. If a cluster persisted throughout the entire analysis interval, the corresponding phase singularities were defined to be associated with an RD. Clusters of phase singularities that did not persist throughout the entire analysis interval were categorized as transient. In all cases, RDs had at least two rotations and lasted at least 200 ms, which is consistent with the definition of RDs in previous publications.[5,34] In addition, for each RD, the dynamic locations of its phase singularities (RD-PS) were tracked to compute RD-PS trajectory length. Pseudo-electrograms in AF were reconstructed by subtracting extracellular potential signals recovered from points 4 cm in the

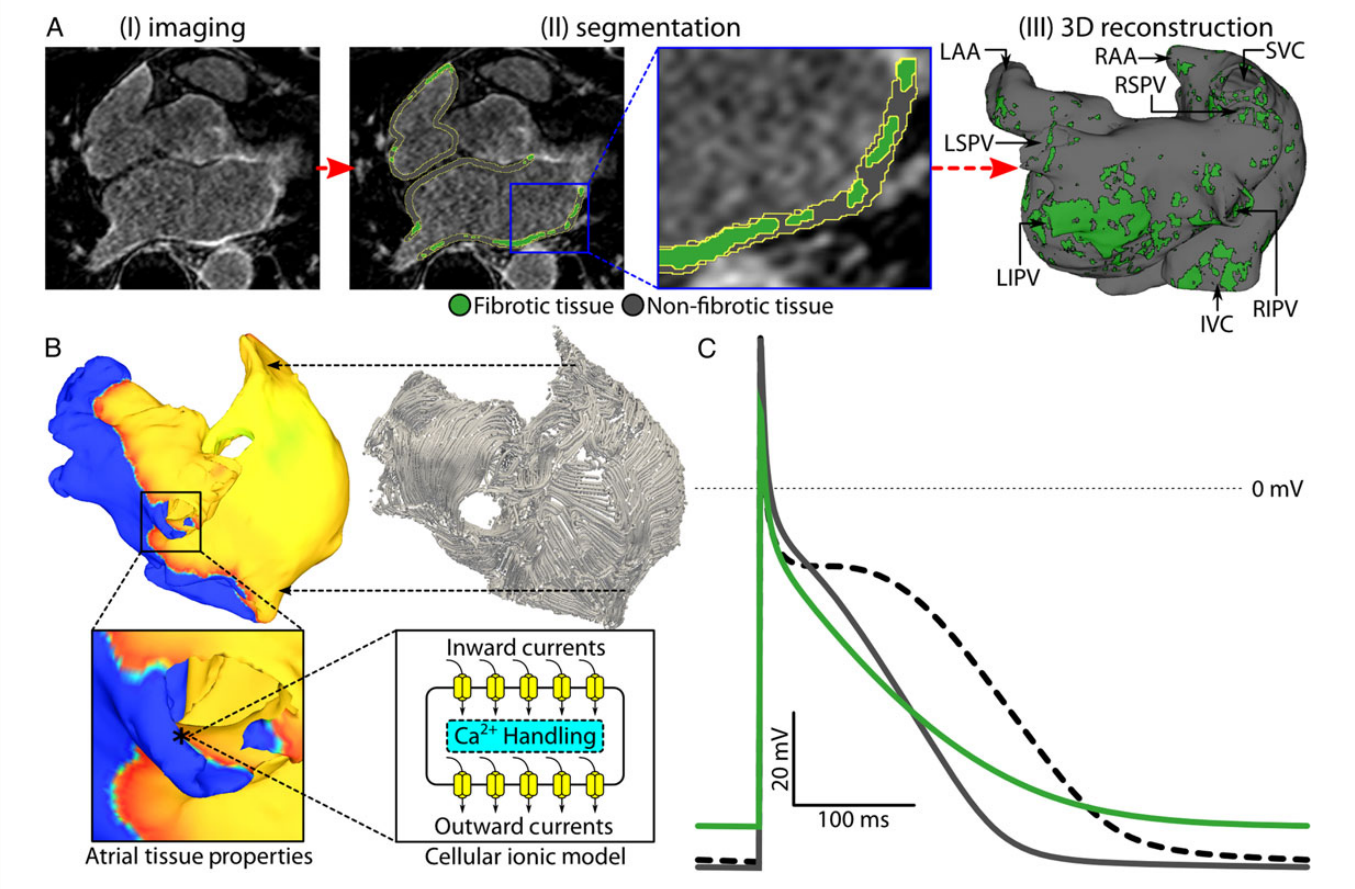


**Figure 1** Model generation. (*A*) Pipeline used to construct image-based models of the fibrotic human atria. (i) Representative LGE-MRI slice of the human atria. (ii) Segmentation of atrial tissue into fibrotic (green) and non-fibrotic (grey) regions based on voxel intensity, as described in Methods. (iii) 3D reconstruction of atrial geometry with anatomical features labelled (RIPV/RSPV/LIPV/LSPV, right/left inferior/superior pulmonary veins; LAA, left atrial appendage; IVC/SVC, inferior/superior vena cava). (*B*) Schematic of multi-scale framework for cardiac electrophysiology modelling. Electrical coupling of atrial cells at the tissue scale mediates propagation of bioelectric impulses, which originate at membrane level (action potentials in the cellular ionic model). Atrial fibre orientations, shown in the top right image, govern the preferential direction of electrical propagation. (*C*) Atrial action potentials obtained at a basic cycle length of 500 ms in fibrotic (green), non-fibrotic tissue (grey), and healthy tissue (dashed).

inferolateral direction from the right and left atrial appendages[37] (additional details in Supplementary material online).

## 2.6 Quantitative characterization of fibrosis spatial pattern

To quantitatively characterize the fibrosis spatial pattern in each patient-derived atrial model, we constructed 3D maps of fibrosis density (FD) and fibrosis entropy (FE). FD and FE values at each location in each atrial model were calculated based on the corresponding characteristics of the local tissue element as well as on those of the surrounding tissue elements within a 2.5 mm radius, which corresponds to the maximum distance between two adjacent voxels in the LGE-MRI scans. The local FD value was calculated as the proportion of fibrotic elements among all elements within the surrounding sub-volume. The local FE in the *i*th element was calculated as the level of disorganization within the surrounding sub-volume, quantified via Shannon entropy:

$$\mathrm{FE} = \sum_{i=1}^{N} \frac{-p_i \ln(p_i)}{N}.$$

$N$ was the number of elements within the sub-volume surrounding the *i*th element. $P_i$ was fraction of elements neighbouring the *i*th element that was a different tissue type than the *i*th element. For example, in the case of a non-fibrotic element with three out of four fibrotic neighbouring elements, the value of $p_i$ was 0.75.

## 2.7 Statistical analysis

Continuous variables are expressed as mean ± SD. Categorical variables are expressed as percentages. Continuous variables were compared using independent-sample non-parametric tests (Wilcoxon Signed-Rank tests). Relationships between continuous variables were assessed using Pearson's correlation coefficient. All statistical tests were two-tailed. A *P*-value of $<0.05$ was considered to indicate statistical significance. Analyses were performed using NCSS 8 (NCSS Statistical Software, Kaysville, UT, USA). A supervised machine learning algorithm was used to identify a polynomial equation that best classified RD and non-RD regions based on combined FD and FE values; this method is detailed in the machine learning protocol subsection in Supplementary material online.

## 2.8 Comparison of simulation results with clinical data

Simulation results regarding the relationship between RD localization and fibrosis pattern distribution in atrial models were compared with clinical mapping data obtained via electrocardiographic imaging (ECGI) in the same PsAF patients. ECGI mapping was performed using a commercially available system (CardioInsight Technologies, Inc., Cleveland, OH) and recorded 10–15 s of AF activity in each patient. Unipolar electrograms were reconstructed from body surface potentials, as previously described.[38]

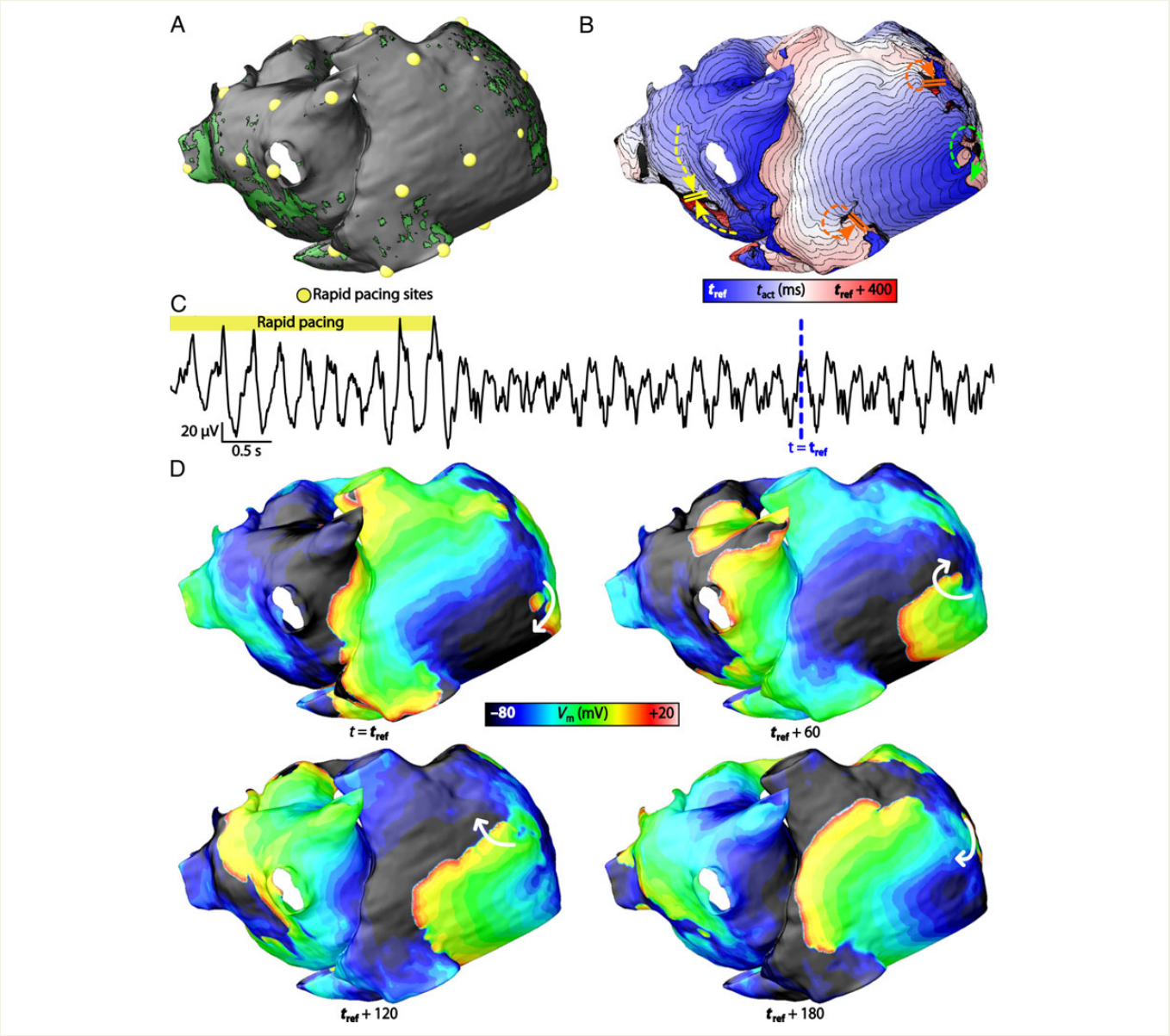


**Figure 2** Induction of AF. (*A*) Locations of 30 sites where rapid pacing was applied for patient model no. 3. (*B*) Activation map of induced AF episode. The location of the RD is in the posterior right atrium (green arrow). There were instances of transient re-entries near the superior and inferior vena cava (red arrows) and conduction block in the posterior left atrium (yellow arrows). (*C*) Pseudo-electrogram recording of the arrhythmia reconstructed by differencing extracellular potential signals from points 4 cm away from the right and left atrial appendages. (*D*) Sequence of transmembrane potential ($V_m$) maps at four different time instants during the AF episode. The reference time ($t_{ref}$) of these $V_m$ maps are indicated by blue dashed arrows in (*C*). The RD in the posterior right atrium is indicated with white arrows.

From unipolar electrograms, local phase was computed to visualize electrical activity during AF, and RD-associated phase singularities were detected using a validated algorithm.[39] More information about the methods underlying ECGI acquisition is available in prior publications.[5,38,39]

# 3. Results

## 3.1 Patient characteristics

The population studied comprise 20 patients (age 52 ± 12 years, 3 women). All patients presented with PsAF, with a maximum uninterrupted duration of 9.3 ± 6.7 months. Five (25%) patients had longstanding PsAF (duration >12 months). LA volume assessed via LGE-MRI was 73 ± 22 mL/m$^2$ (normalized to body surface area); biatrial and LA-only fibrosis burdens were 19.7 ± 5.7 and 22.8 ± 6.1%, respectively. LA fibrosis burden was categorized as Utah Stage I in 0 (0%), Stage II in 7 (35%), Stage III in 9 (45%), and Stage IV in 4 (20%) patients. The biatrial fibrosis burden was not correlated to the LA volume ($R = 0.38$, $P = 0.07$) or age ($R = 0.34$, $P = 0.10$). A summary of patient characteristics is presented in Supplementary material online, *Table S2*.

## 3.2 Patient-derived model generation and *in silico* AF induction

The generation of personalized 3D atrial models was successful for all 20 patients. The *in silico* stimulation protocol induced AF in 13 out of 20

patient-derived atrial models. AF-inducible models had significantly larger fibrosis burdens than non-inducible models (16.1 ± 4.4 vs. 21.6 ± 5.6, $P = 0.04$). In the 13 inducible patient-derived models, the number of pacing sites from which AF could be induced was highly variable (mean 5/30 sites, ranging from 1 to 20) and correlated to biatrial fibrosis burden ($R = 0.62$, $P < 0.001$). Patient-derived models in which AF was induced had significantly larger APD gradients (see Supplementary material online, *Figure S1*) (54.0 ± 5.5 vs. 42.0 ± 7.0 ms, $P < 0.05$) and total atrial activation times (381.8 ± 45.3 vs. 338.6 ± 41.9 ms, $P < 0.05$) in sinus rhythm than those that were not inducible for arrhythmia. Supplementary material online, *Table S3* details the differences in patient-derived model characteristics and electrophysiological variables from simulations in models inducible and non-inducible for AF.

## 3.3 Characteristics of simulated AF episodes

*In silico* AF induction by programmed electrical stimulation and the subsequent activation patterns are illustrated in *Figure 2*. In all 13 AF-inducible models, and for all AF morphologies, AF was driven by persistent RDs that formed in only a few atrial regions (*Figure 2B*, green arrow); there were 1 to 5 such RDs in each model (average 2.7 ± 1.5). The activation pattern distal from each persistent RD was disorganized and fibrillatory, with multiple instances of transient re-entry (*Figure 2B*, red arrows) and areas of conduction block (*Figure 2B*, yellow arrows). The complex activation pattern observed during simulated AF was associated with irregular pseudo-electrograms (*Figure 2C*). $V_m$ maps in *Figure 2D* detail an episode of AF maintained by an RD in the posterior right atrium of patient model no. 3 (white arrows). When myocyte membrane kinetics in fibrotic regions were represented with the same atrial action potential model used in non-fibrotic regions in all 13 AF-inducible models, reapplication of programmed electrical stimulation at the 30 distinct sites did not induce arrhythmia in any of the models (see Supplementary material online, *Figure S2*).

*Figure 3A* and *C* show $V_m$ maps during AF in models no. 1 and no. 16, respectively. The dynamic locations of RD-PSs over time for these AF episodes show that RDs persisted in spatially confined regions. For all unique AF morphologies observed in all models, the maximum RD-PS trajectory length was <10 mm (average: 7.57 ± 2.33 mm). *Figure 3B* and *D* show RD-PS trajectories for all unique AF morphologies observed in models no. 1 and no. 16, respectively (red circles correspond to AF episodes shown in *Figure 3A* and *C*).

## 3.4 Local fibrosis characteristics at re-entrant driver sites

To better understand the dynamics of RDs induced in each atrial model, we analysed the relationship between RD-PSs and the fibrosis spatial pattern. *Figure 4A* shows the activation sequence (left) of an AF episode maintained by an RD near the inferior vena cava in model no. 1, with inset panels (right) highlighting $V_m$ maps of the same RD and its RD-PS locations at four different time instants, along with the outlines of fibrotic tissue. At these time instants and throughout the re-entry (*Figure 4B*), the RD-PS dynamic location was along a trajectory that followed a boundary between fibrotic and non-fibrotic tissue (*Figure 4B*).

Maps of the distributions of fibrosis metrics FD and FE in each atrial model were used to quantify the spatial characteristics of the regional fibrosis pattern where RDs persisted. *Figure 5A* and *C* show the distribution of fibrotic tissue in models no. 6 and no. 8 (left); inset panels present zoomed-in views of FD and FE maps together with RD-PS trajectories and outlines of fibrotic regions (right). As the figure demonstrates, RD-PSs were located in atrial tissue with relatively high values of both FD and FE (>0.45, corresponding to orange coloured regions). Regions with this characteristic corresponded to a subset of fibrotic tissue boundaries with extensive intermingling between fibrotic and non-fibrotic tissues. RD-PSs were not observed in regions of dense fibrotic tissue (e.g. sites marked by asterisks in *Figure 5A* and *C*). *Figure 5B* and *D* show time series plots of FD and FE values at RD-PS locations during one second of AF for the episodes shown in *Figure 5A* and *C*, respectively.

In the 13 AF-inducible atrial models, regions containing the RD-PS trajectories (i.e. RD-PS regions) had significantly higher FD (interquartile range [IQR]: 0.59–0.769 vs. 0.00–0.33, $P < 0.05$) (*Figure 6A*) and FE (IQR: 0.42–0.60 vs. 0.00–0.40, $P < 0.05$) (*Figure 6B*) values compared with regions where RD-PSs did not occur (i.e. non-RD-PS regions). RD-PS regions had an FD of 0.63 ± 0.17 and FE of 0.51 ± 0.14 (*Figure 6C*). Non-RD-PS regions had an FD of 0.13 ± 0.19 and FE of 0.18 ± 0.22 (*Figure 6D*).

To examine the sensitivity of RD localization to the signal intensity threshold value used to discriminate fibrotic from non-fibrotic tissue in the LGE-MRI scans, we repeated the simulations with the models that were originally non-inducible for AF using a different signal intensity threshold. Specifically, we decreased the signal intensity threshold on average by 5.4%, which increased the biatrial fibrosis burden from 16.1 ± 4.4 to 21.5 ± 4.2%. After application of programmed electrical stimulation, AF was induced in five of the seven models. The RDs that perpetuated AF still persisted in spatially confined regions, characterized with significantly higher fibrosis density (IQR: 0.70–0.92 vs. 0.00–0.33, $P < 0.05$) and entropy (IQR: 0.25–0.51 vs. 0.00–0.40, $P < 0.05$) than non-RD-PS regions (see Supplementary material online, *Figure S3*). Furthermore, activation times and APD gradients in sinus rhythm in these five AF-inducible models with the new fibrosis distributions increased to 397.3 ± 70.9 and 54.0 ± 3.0 ms, respectively, becoming similar to those in the original 13 AF-inducible models (381.8 ± 45.3 and 54.0 ± 5.5 ms, respectively, $P = 0.67$); see also Supplementary material online, *Figure S1C*. These results demonstrate that increasing the spatial extent of the fibrotic regions resulted in increases in activation times, APD gradients, and AF inducibility.

A supervised machine learning algorithm was used to identify a polynomial equation that best classified RD-PS and non-RD-PS regions based on FD and FE values (*Figure 7A*; algorithm details in Supplementary material online). Receiver operating characteristic analysis demonstrated that the resulting classification had minimal false-positive selection of RD-PS regions [area under the curve (AUC) = 0.91] (*Figure 7B*); precision-recall analysis indicated that the approach had minimal false-negative selection of non-RD-PS regions (AUC = 0.84) (*Figure 7C*). Taken together, the latter two analyses demonstrated that our approach to identifying RD-PS regions was robust to over- and under-fitting. To test the sensitivity of the machine learning classification to the kernel size radius used to calculate FD and FE, we increased the kernel size radius by 50% and repeated the classification algorithm. Machine learning classification remained robust, as assessed by the receiver operating characteristic (AUC = 0.91) and precision-recall curves (AUC = 0.86) (see Supplementary material online, *Figure S4*). Atrial tissue with the specific FD and FE characteristics identified by the machine learning algorithm (i.e. Pro-RD regions with FD/FE properties in the green region of *Figure 7A*) corresponded to a subset of fibrotic region boundary zones (*Figure 7D*). These Pro-RD regions (i.e. regions with high FD and FE values) had significantly larger APD variance than other regions of the atria

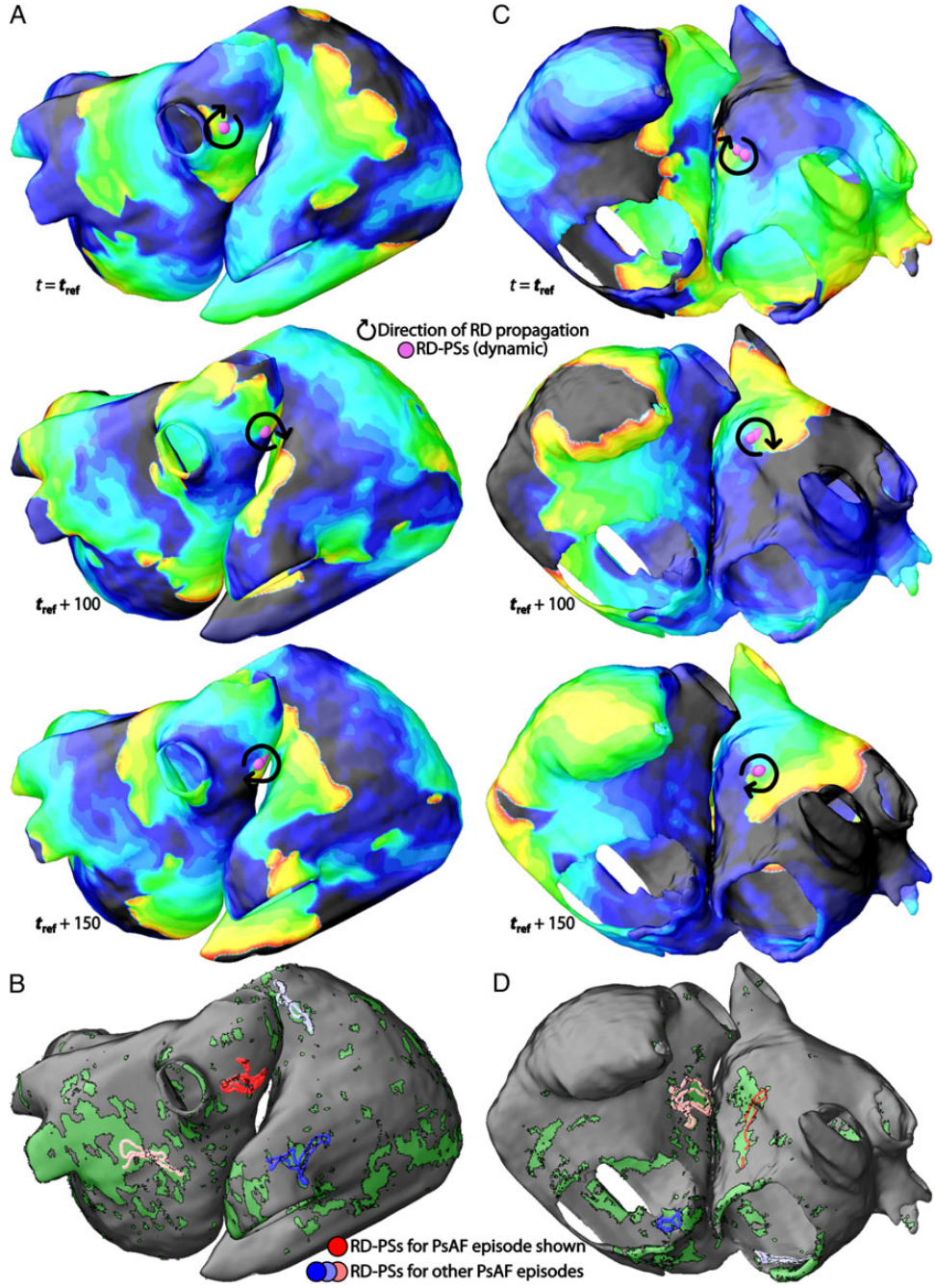


**Figure 3** Locations of RD-PSs. (*A*) Sequence of $V_m$ maps during AF for atrial model no. 1. The locations of RD-PSs and direction of RD propagation are indicated with purple circles and black arrows, respectively. (*B*) The aggregate locations of RD-PSs for all AF episodes observed in patient model no. 1 (distinct colours reflect distinct AF morphologies). Red circles correspond to RD-PSs in the AF episode in (*A*). (*C*) Sequence of $V_m$ maps during AF for patient model no. 16. (*D*) The aggregate locations of RD-PSs for all AF episodes in patient model no. 16. Red circles correspond to the RD-PSs in the AF episode in (*C*).

(101.1 vs. 90.2 ms; Levene statistic = 308 586, $P < 0.05$). This suggests that APD gradients are larger in regions characterized by high FD and FE values. Although only 13.79 $\pm$ 4.93% of all atrial tissue had this characteristic fibrosis spatial pattern, such tissue was present in 83.50 $\pm$ 2.35% of all locations where RD-PSs occurred dynamically in the 13 AF-inducible patient-derived atrial models.

Finally, the predicted Pro-RD regions, as identified from the above simulation results by the machine learning algorithm, were compared with clinically observed regions of most frequent RD-PS occurrence. *Figure 7E* presents example ECGI maps from two patients from the cohort used in this study. When regions with the Pro-RD fibrosis spatial pattern, as identified by machine learning trained on simulation results, were mapped from the patient-derived atrial geometry onto the corresponding ECGI atrial geometry (*Figure 7E*), we observed significant co-localization of those regions (marked by black cross-hatching) with regions where RD-PSs were observed most frequently during clinical

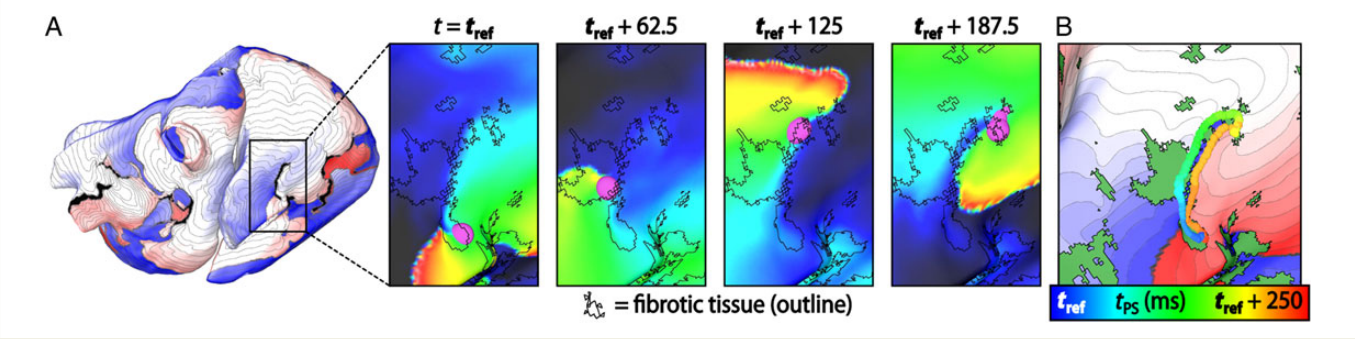


**Figure 4** Dynamic (i.e. time-varying) locations of RD-PS during an AF episode. (*A*) Activation map showing an RD in patient model no. 1 near the inferior vena cava. Inset panels show a zoomed-in view of $V_m$ maps in the vicinity of the RD location at four time instants (as labelled). RD-PSs are marked with purple circles. The fibrotic tissue region boundaries are indicated by black outlines. (*B*) Trajectory of RD-PS movement over time superimposed on the activation map of the re-entry and the fibrosis spatial pattern (green regions). Each discretely coloured circle marks an RD-PS location at a unique instant of time.

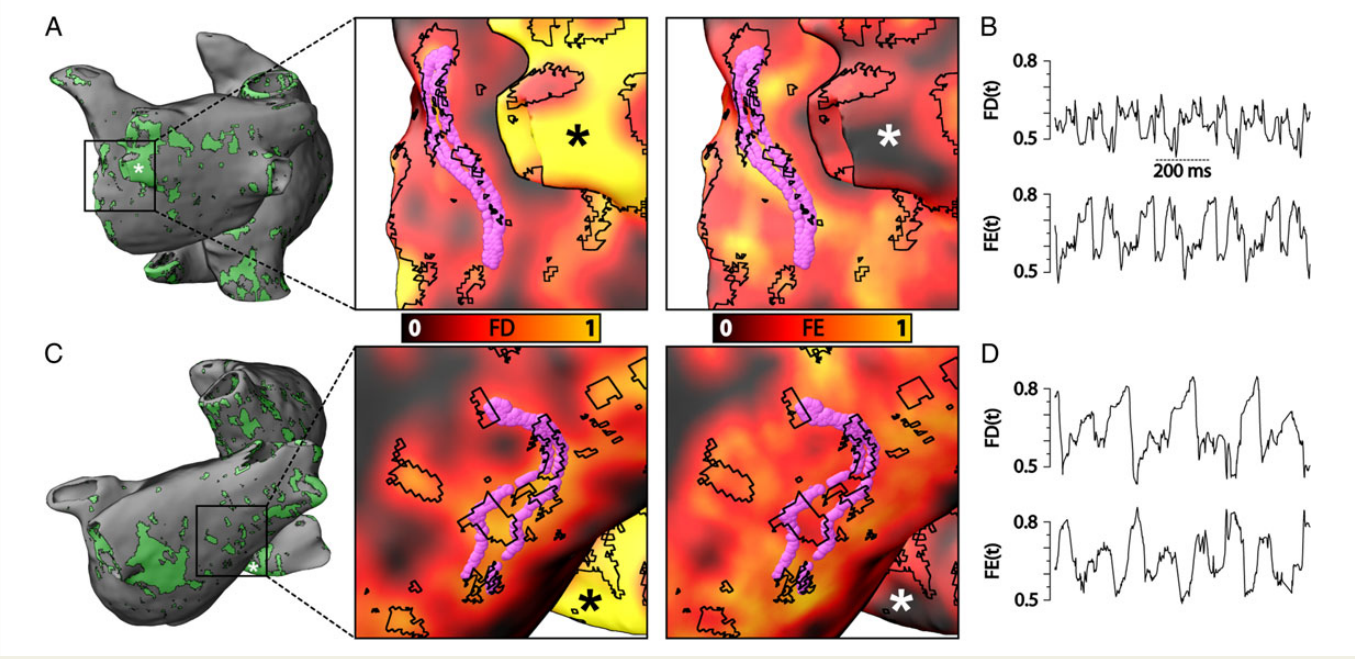


**Figure 5** FD and FE characteristics at RD-PS locations. (*A*) Left panel shows the fibrotic tissue distribution near the left pulmonary veins for patient model no. 6, where an RD was observed. Inset panels show maps of FD (left) and FE (right) in this area; fibrotic tissue boundaries are outlined in black. The locations of RD-PSs at each time instant are indicated with purple circles. RD-PSs were dynamically located in regions with high FD and FE values (orange areas). Black and white asterisks mark regions of dense fibrotic tissue with high FD, but low FE—RD-PSs were not observed in these areas. (*B*) Time series plot of FD and FE at RD-PS locations for the case shown in (*A*); FD and FE values range from 0.45 to 0.8. (*C*) Left panel shows the fibrotic tissue distribution in the posterior left atrium for patient model no. 8, where an RD was observed in an AF episode. Inset panels show maps of FD and FE, fibrotic tissue boundaries, RD-PS locations, and regions of dense fibrotic tissue as described in (*A*). (*D*) Time series plot of FD and FE at RD-PS locations for the case shown in (*C*); FD and FE values range from 0.45 to 0.8.

mapping (red areas). Two additional examples are presented in Supplementary material online, *Figure S5*. Overall, 56.7 $\pm$ 9.1% of all areas where RD-PD were observed in ECGI maps were located in Pro-RD areas.

## 4. Discussion

To the best of our knowledge, this is the largest 3D, biophysically detailed computational modelling study ever undertaken on atrial electrophysiology. In 20 patient-derived atrial models with individualized fibrosis distributions derived from LGE-MRI, we showed that (i) AF is inducible by programmed electrical stimulation in models that have a sufficient amount of fibrosis, (ii) the induced AF is perpetuated by RDs that persist in spatially confined regions, and (iii) the latter regions constitute boundary zones between fibrotic and non-fibrotic tissue that are characterized with high fibrosis density and entropy values.

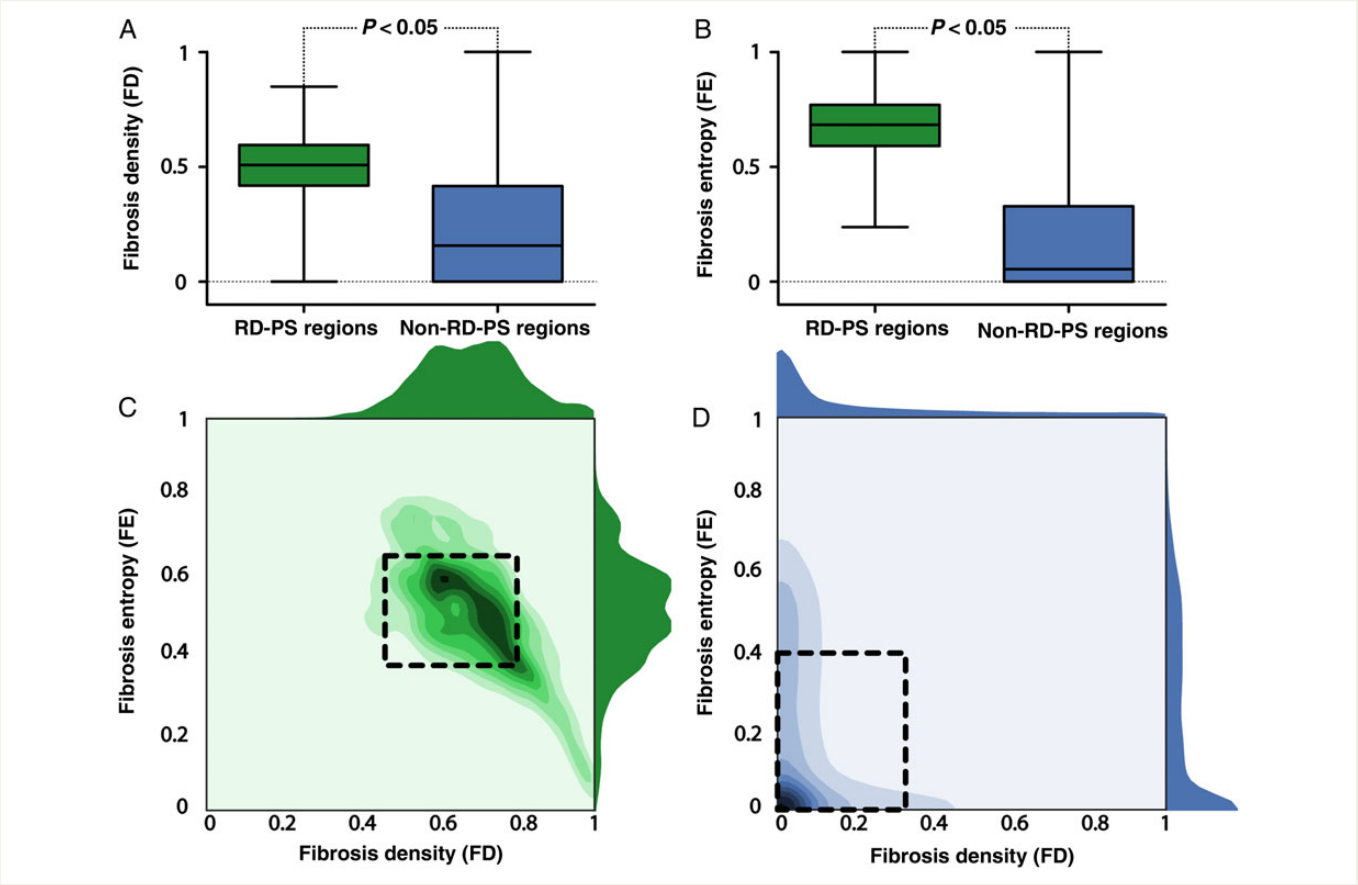


**Figure 6** Summary of FD and FE characteristics at RD-PS locations for all AF episodes in all atrial models. (*A*) Boxplot of FD values in regions of atrial tissue where RD-PSs persisted (RD-PS regions, $n = 20\,767$) and where RD-PSs did not occur (non-RD-PS regions, $n = 1\,657\,133$) for all AF episodes in all atrial models. FD in RD-PS regions is significantly higher than FD in non-RD-PS regions (IQR: 0.59–0.769 vs. 0.00–0.33, $P < 0.05$). (*B*) Boxplot of FE at RD-PS regions and non-RD-PS regions for all AF episodes in all atrial models. FE values in RD-PS regions ($n = 20\,767$) are significantly higher than those in non-RD-PS regions ($n = 1\,657\,133$, IQR: 0.42–0.60 vs. 0.00–0.40, $P < 0.05$). (*C*) 2D Histogram of the FE and FD values at RD-PS regions for all AF episodes in all atrial models. Right and top panels show the respective 1D histogram of just FE (right) and FD (top). Boxed region encloses FE and FD values ($0.37 \leq FE \leq 0.65$; $0.46 \leq FD \leq 0.80$) within 1 S.D. of the mean of the FD and FE in RD-PS regions. (*D*) 2D Histogram of FE and FD values at non-RD-PS regions for all AF episodes in all atrial models. Right and top panels show the respective 1D histogram of just FE (right) and FD (top). Boxed region encloses FE and FD values ($0 \leq FE \leq 0.40$; $0 \leq FD \leq 0.32$) within 1 S.D. of the mean of the FD and FE in non-RD-PS regions.

## 4.1 Generation of patient-derived atrial models and AF induced in the fibrotic substrate

The characteristics of the studied population were similar to those of the usual population presenting with PsAF in terms of age, gender, and PsAF duration, as well as atrial volume and fibrosis burden.[8,9,40] The method used to segment fibrosis from LGE-MRI data is based on prior reports,[7,16,40] and the relationship between fibrosis burden and PsAF duration is consistent with past studies.[8] In the atrial models constructed from the patient LGE-MRI scans, representation of atrial electrophysiology at the cell, tissue, and organ level in fibrotic and non-fibrotic regions were based on a large body of evidence from human,[24] animal,[26–28] and computational studies.[20–22] Arrhythmogenic properties of the fibrotic substrate were evaluated by programmed electrical stimulations using a dynamic pacing train delivered from a large number of locations throughout the atria. Using this protocol, AF was induced in 13/20 models, which contained a greater amount of fibrosis than the 7 non-inducible models. No arrhythmia was induced in any model when the fibrotic regions were represented with tissue-level remodelling only, via reduction in intercellular coupling and increase in longitudinal transverse anisotropy. Thus, cell-level changes in fibrotic regions, such as those in excitability and refractoriness, need to be incorporated to properly recapitulate the arrhythmogenic propensity of the fibrotic substrate in patient-derived atrial models.

After pacing tissue at normal sinus rhythm rates at the sinoatrial node, patient-derived models inducible for AF had APD gradients and total atrial activation times that were significantly larger than those in non-inducible models. Thus, assessing APD gradients and total atrial activation times may be beneficial in probing the arrhythmogenic propensity of the fibrotic substrate in a clinical setting without inducing AF.

AF was not inducible in 7 of the 20 patient-derived models. The fibrosis burden in the 7 non-inducible models was significantly smaller than that in the 13 AF-inducible models. However, the signal intensity threshold used here to discriminate fibrotic from non-fibrotic tissue has a level of uncertainty associated with it; it is dependent on scan quality and operator experience.[7] This could potentially decrease the

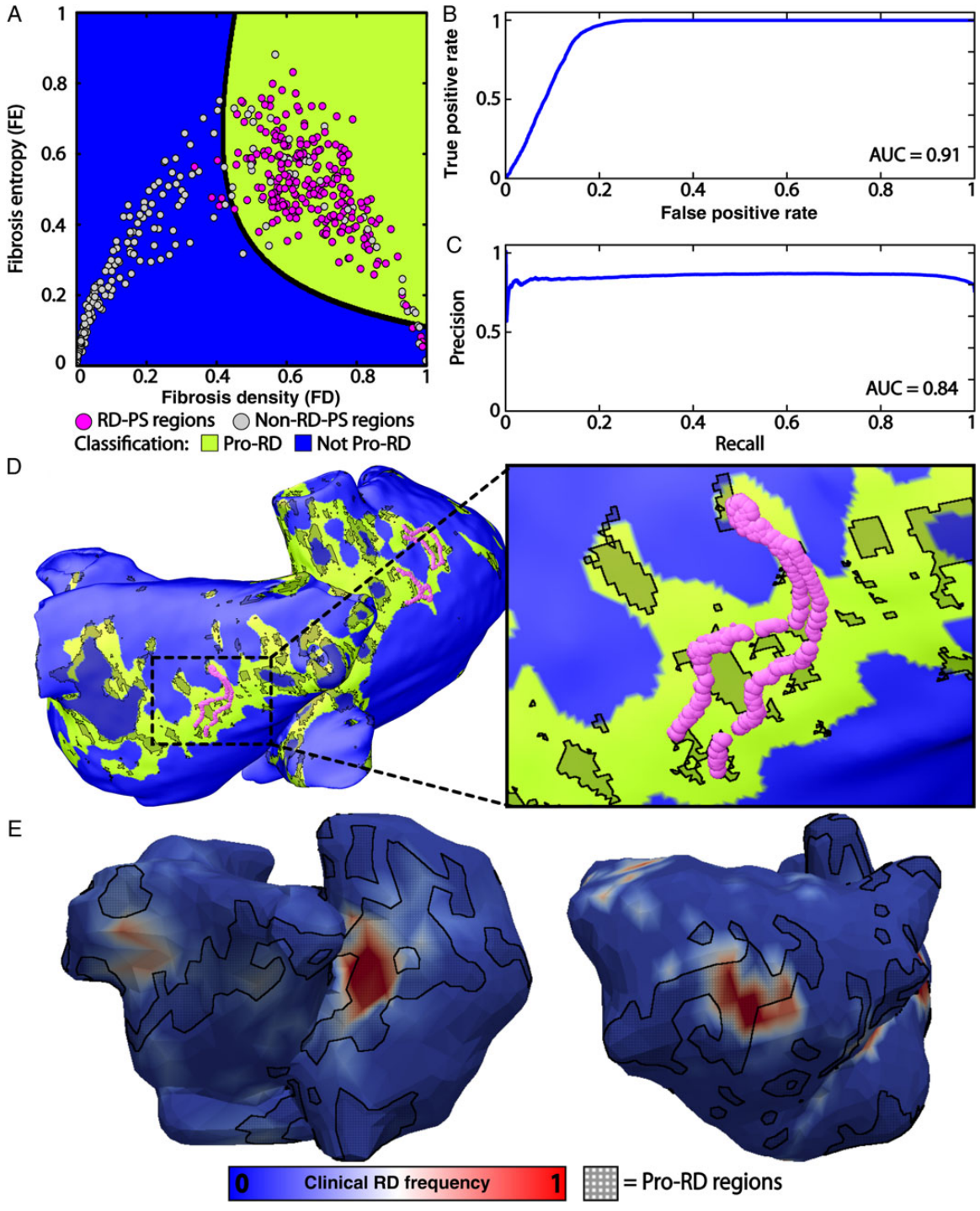


**Figure 7** Machine learning classification of RD-PS and non-RD-PS regions based on FD and FE. (*A*) Classification of RD-PS and non-RD-PS regions. The polynomial equation that separated RD-PS (purple circles) and non-RD-PS regions (yellow circles) is indicated with a black line. The FD and FE values that characterized RD-PS regions and non-RD-PS regions are indicated in green (Pro-RD) and blue (Not Pro-RD), respectively. (*B*) Receiver operating characteristic analysis of the machine learning algorithm. The AUC for this plot was 0.91. (*C*) Precision-recall analysis of the machine learning algorithm. The AUC for this plot was 0.84. Together, (*B*) and (*C*) indicate robust classification. (*D*) Location of RD-PSs in patient model no. 8 overlaid on the regions of the atria with the characteristic FD and FE values predicted to contain RD-PSs (green). 13.79 $\pm$ 4.93% of all atrial tissue had this characteristic fibrosis pattern; 83.50 $\pm$ 2.35% of all RD-PSs were in these regions. (*E*) Comparison with clinical results. Example atrial ECGI maps are shown for patients no. 8, left, and no. 5, right. Red colour indicates regions of greatest frequency of RD-PSs occurrence. Pro-RD regions (regions favourable to RD-PS localization, marked with black cross-hatching), as identified by machine learning trained on simulation results, were transferred from the patient-derived atrial geometry and onto the ECGI atrial geometry of the same patient for comparison.

extent of the fibrotic regions in these models and make them less susceptible to arrhythmia. To test this hypothesis, we decreased the signal intensity threshold discriminating fibrotic tissue on average by 5.4% in these seven models. Following programmed electrical stimulation in these originally non-inducible models, AF was induced in five of seven cases. In addition, activation times and APD gradients in the 5 newly AF-inducible models with re-calculated fibrosis distribution increased and became similar to those in the original 13 AF-inducible models. These results demonstrate that increasing the fibrosis burden is the primary cause of increased AF inducibility in this study. The remaining two non-inducible models had a small amount of fibrotic remodelling even after changing the signal intensity threshold, indicating that mechanisms other than arrhythmogenesis arising from fibrosis were most likely responsible for perpetuating AF in these patients.

The RDs induced in the five newly AF-inducible models still persisted in spatially confined regions characterized with high FD and FE values, which echoes findings in optical mapping[15] and ECGI studies.[41] This suggests that the central finding of our study is relatively insensitive to the inherent limitations of LGE-MRI—if models were reconstructed using a different segmentation threshold, the absolute locations of RDs would potentially change, but their relation to the underlying fibrosis spatial pattern would be the same.

## 4.2 Characteristics of simulated AF episodes induced by programmed electrical stimulation

The analysis of AF dynamics in inducible atrial models showed a combination of sustained RDs, transient re-entries, wave collisions, and functional blocks all of which have been described in mapping studies of PsAF in humans.[42] These complex activation patterns were associated with irregular pseudo-electrograms, which were qualitatively similar to clinical electrograms of PsAF.[43] Our results confirm that PsAF can be perpetuated by RDs that dynamically emerge in a limited number of locations (1–5 unique RD domains per patient; average: $2.69 \pm 1.54$). In simulations, RDs persisted for the duration of the entire simulation period (2.5 s). Phase singularities associated with each RD were not stationary but meandered within spatially restricted regions (average extent: $7.57 \pm 2.33$ mm). These findings are consistent with observations of RD dynamics in PsAF from recent clinical studies in terms of the number, size, and stability of RD domains. Haïssaguerre *et al.*[5] used inverse electrocardiography (ECGI) in pre-ablation PsAF patients and identified between two and six distinct RD domains in each individual. Furthermore, regions where RDs were observed most frequently were found to be small and therefore amenable to catheter ablation.[5,41] Likewise, FIRM-guided ablation studies[6] in PsAF patients reported a small number of drivers (total of $2.2 \pm 1.0$ per patient, although re-entrant and focal sources were not separately reported), with RDs that meandered within compact regions (1–2 $cm^2$).

Consistent with the goals of the research, the present study did not include, by design, automatic focal activity, so that the contribution of the fibrotic substrate to AF can be assessed in the absence of all other confounding factors. We used programmed electrical stimulation and explored the relationship between fibrosis distribution and the locations of the RD(s) induced from each pacing site in each patient-derived model. Although in patients with AF there would also be contributions to overall activity from paroxysmal triggered activations and simultaneously occurring RDs,[5] we expect nonetheless that our primary finding that RDs persist in spatially confined regions characterized with high FD and FE values would remain valid. We expect, however, that in PsAF patients RD-RD interactions and RD interactions with focal sources would have de-stabilizing influence, shortening RD residence at a particular spatial location. Specifically, we expect that a focal driver or impinging activity from another RD might dislodge an RD from one fibrotic region, leading it to re-anchor to a different location with the same characteristics of the fibrosis pattern. Such dynamics of PsAF would be consistent with findings from ECGI,[5] where RDs occur most frequently in spatially restricted regions but also move between such regions, with shorter lifespans at each anchoring site (typically $<1$ s).

## 4.3 Characteristics of the fibrosis pattern in regions where RDs persist

Fibrosis architecture is highly variable from patient to patient in the PsAF population, as well as from region to region within the atria of a given patient.[8,9] In our simulations of AF in the fibrotic atria, RDs were only observed in a limited number of atrial sites. Therefore, we hypothesized that the fibrosis spatial pattern necessary to anchor re-entry was highly specific. For all induced AF episodes in all atrial models, the confined regions within which the RD-PSs meandered had a consistent fibrosis spatial pattern, characterized by high values of both FD and FE ($0.37 \leq FE \leq 0.65$; $0.46 \leq FD \leq 0.80$). This combination of metrics corresponds to atrial locations with a high degree of intermingling between fibrotic and non-fibrotic tissue. RD-PSs were conspicuously absent from both completely non-fibrotic sites and regions of deep fibrosis (i.e. locations with high FD and low FE, such as those marked by asterisks in *Figure 5*). This is a key observation, because it expands upon the recent clinical finding that RDs identified by ECGI are co-localized with fibrosis boundary zones identified by LGE-MRI.[16] Our results demonstrate that only a limited subset of fibrosis border zones has the characteristics (i.e. high FD and high FE) needed to sustain RDs. The use of sophisticated machine learning tools enabled us to devise a sensitive and specific classification scheme capable of pinpointing the combination of FD and FE metric values associated with RD localization. Overlaying machine learning-predicted Pro-RD areas on clinical ECGI maps displaying areas where RD-PSs were observed most frequently in each patient's atria showed very good co-localization. This supports the predictions of the simulations regarding the relationship between fibrosis spatial pattern and the locations of re-entrant drivers of AF. Indeed, given that nearly 60% of re-entrant drivers identified clinically fell in machine learning-predicted regions covering on average only ~13% of the atrial volume, the correspondence between simulation results and clinical data can be considered very good. Over all of the models, this co-localization is not, however, excellent because ECGI maps also reflect, in the dynamics of the RD-PSs, the influence of the presence of focal sources and other simultaneously occurring re-entrant drivers, as discussed above.

Regions with both high FD and high FE are a potent substrate for the initiation and perpetuation of RDs, because such locations are associated with steep spatial gradients in excitability, refractoriness, and APD, rendering them highly prone to conduction failure[10] due to the extensive intermingling of fibrotic and non-fibrotic tissue. As part of the border zones of fibrotic remodelling, these RD regions are in contact with both non-fibrotic tissue, which allows propagating wavefronts to rapidly pivot around zones of functional block,[44] and with more fibrotic regions that ensure sufficient conduction slowing[11–13] to sustain re-entry. The average size of the RD perpetuation regions in our study ($7.57 \pm 2.33$ mm) is consistent with findings from previous simulation

and experimental work, demonstrating that RDs are attracted to and/or anchored by inhomogeneties of a similar spatial scale (4.5–10 mm) resulting from gradients in ion channel expression,[45] APD,[46] or microfibrosis.[15]

### 4.4 Clinical perspectives

Knowledge regarding the link between dynamic RD localization and the spatial characteristics of the fibrotic substrate, as acquired in this study, has important implications for clinical strategies to manage and treat PsAF in patients. Multiple centres have reported that ablation of RD-harbouring sites can terminate PsAF or convert it to a more clinically manageable tachycardia,[5,6] but it remains unclear why this type of targeting has therapeutic value. Our results suggest that this success may be attributable to the fact that such ablations homogenize the tissue in an RD-anchoring region, rendering it more like a deeper fibrotic region with less interdigitation of fibrotic and non-fibrotic tissue (i.e. lower values of FD/FE). It is also conceivable that locations with FD/FE favouring RD localization, as identified by processing the LGE-MRI images, could be directly targeted for ablation, consistent with current clinical concepts of substrate modification[47] for PsAF ablation. Of note, the total amount of atrial tissue with such high FD/FE combination in each patient was relatively small (13.8 $\pm$ 4.9% of the atria). RDs in our study were found to persist in not all, but a portion of the regions with high FD/FE (see *Figure 7D*); the simulation results were supported by the comparison with the clinical ECGI maps. It is likely that pacing from other sites, in addition to the 30 used in each patient-derived model, will result in the formation of persistent RDs in the reminder of high FD/FE tissue. We further speculate that following ablation of a region sustaining an RD, new emergent RDs will localize to sites with the same (high FD/FE) fibrosis spatial characteristics. As such, the percentage cited above should be interpreted as the theoretical maximum amount of tissue that must be ablated to eliminate the RD-perpetuating properties of the fibrotic substrate. Future work will be needed to determine whether and how this tissue subset could be further narrowed towards achieving truly optimal ablation lesion sets.

### 4.5 Study limitations

One limitation of this study is related to the reconstruction of personalized models from LGE-MRI data, in which LGE-MRI abnormalities are taken as surrogates for fibrosis. Despite histological validation in a small number of patients,[48] it remains debated whether LGE-MRI abnormalities truly represent fibrosis. Another inherent limitation of LGE-MRI is the inability to detect diffuse, homogeneously distributed fibrosis or microfibrosis,[49] which have been shown to anchor micro-re-entries.[15] Although these limitations require a careful evaluation when considering the potential use of personalized MRI-tailored ablation therapy, we believe they do not impact the main finding of our study that RDs persist in regions with greater levels of FD and FE.

In addition to correctly representing the arrhythmogenic propensity of the fibrotic substrate, modelling AF dynamics in patients may need to incorporate other aspects of electrophysiological remodelling. Specifically, inflammation[50] and heart failure[12] have been shown to induce changes in ionic current expression and modify myocyte APDs.[12,50,51] Furthermore, Haissaguerre *et al.*[5] and Narayan *et al.*[6] have shown that focal impulses alone can sustain AF in patients with persistent forms with this disease. Inclusion of these components may be necessary to match AF dynamics in patient-derived models to clinical characteristics, especially in cases where patients do not have LGE-MRI abnormalities or low-voltage regions in the atria.

In this study, fibrotic tissue is represented with remodelled electrophysiology, anisotropy, and conduction properties based on evidence from experimental studies. Previous studies have represented fibrotic remodelling with discontinuous finite elements,[52] single elements modelled as passive resistors,[53] or the effect of myofibroblasts.[21] We believe that our representation of fibrotic remodelling is the most appropriate for use in patient-derived models that are based on and have the resolution of clinical imaging data since it incorporates experimentally derived parameter values and ensures computational tractability.

## 5. Conclusion

We demonstrated that reconstruction of personalized 3D atrial models with individualized fibrosis patterns from LGE-MRI is feasible. Dynamic pacing from a number of locations was able to induce AF in atrial models that included sufficient amounts of fibrosis. Simulations demonstrated that AF in the fibrotic substrate is perpetuated by RDs localized in boundary zones between fibrotic and non-fibrotic tissue that are characterized with high fibrosis density and entropy. These results provide new insights into the mechanisms of PsAF perpetuation and pave the way towards an MRI-based approach for the personalization of clinical management in patients with PsAF.

## Supplementary material

Supplementary material is available at *Cardiovascular Research* online.

**Conflict of interest:** M.H., M.H., R.D., and P.J. are stockholders in CardioInsight Inc. E.V. and N.T. are cofounders of CardioSolv, LLC. CardioInsight and CardioSolv were not involved in this research. Other co-authors declare no conflicts of interest.

## Funding

This work was supported by the French National Research Agency (ANR-11-EQPX-0030, ANR-10-IAHU-04); Johns Hopkins Medicine Discovery Fund [to N.A.T.]; National Institutes of Health Pioneer Award DP1-HL123271 [to N.A.T.]; National Science Foundation CDI 1124804 [to N.A.T.] and Graduate Research Fellowship [to S.Z.]; and ARCS Foundation Award [to S.Z.].

## References

1. Andrade J, Khairy P, Dobrev D, Nattel S. The clinical profile and pathophysiology of atrial fibrillation: relationships among clinical features, epidemiology, and mechanisms. *Circ Res* 2014;**114**:1453–1468.
2. Verma A, Jiang CY, Betts TR, Chen J, Deisenhofer I, Mantovan R, Macle L, Morillo CA, Haverkamp W, Weerasooriya R, Albenque JP, Nardi S, Menardi E, Novak P, Sanders P, Investigators SAI. Approaches to catheter ablation for persistent atrial fibrillation. *N Engl J Med* 2015;**372**:1812–1822.
3. Nattel S, Guasch E, Savelieva I, Cosio FG, Valverde I, Halperin JL, Conroy JM, Al-Khatib SM, Hess PL, Kirchhof P, De Bono J, Lip GY, Banerjee A, Ruskin J, Blendea D, Camm AJ. Early management of atrial fibrillation to prevent cardiovascular complications. *Eur Heart J* 2014;**35**:1448–1456.
4. Mandapati R, Skanes A, Chen J, Berenfeld O, Jalife J. Stable microreentrant sources as a mechanism of atrial fibrillation in the isolated sheep heart. *Circulation* 2000;**101**:194–199.
5. Haissaguerre M, Hocini M, Denis A, Shah AJ, Komatsu Y, Yamashita S, Daly M, Amraoui S, Zellerhoff S, Picat MQ, Quotb A, Jesel L, Lim H, Ploux S, Bordachar P, Attuel G, Meillet V, Ritter P, Derval N, Sacher F, Bernus O, Cochet H, Jais P, Dubois R. Driver domains in persistent atrial fibrillation. *Circulation* 2014;**130**:530–538.
6. Narayan SM, Krummen DE, Shivkumar K, Clopton P, Rappel WJ, Miller JM. Treatment of atrial fibrillation by the ablation of localized sources: CONFIRM (Conventional Ablation for Atrial Fibrillation With or Without Focal Impulse and Rotor Modulation) trial. *J Am Coll Cardiol* 2012;**60**:628–636.
7. Oakes RS, Badger TJ, Kholmovski EG, Akoum N, Burgon NS, Fish EN, Blauer JJ, Rao SN, DiBella EV, Segerson NM, Daccarett M, Windfelder J, McGann CJ, Parker D, MacLeod RS, Marrouche NF. Detection and quantification of left atrial structural

remodeling with delayed-enhancement magnetic resonance imaging in patients with atrial fibrillation. *Circulation* 2009;**119**:1758–1767.
8. Marrouche NF, Wilber D, Hindricks G, Jais P, Akoum N, Marchlinski F, Kholmovski E, Burgon N, Hu N, Mont L, Deneke T, Duytschaever M, Neumann T, Mansour M, Mahnkopf C, Herweg B, Daoud E, Wissner E, Bansmann P, Brachmann J. Association of atrial tissue fibrosis identified by delayed enhancement MRI and atrial fibrillation catheter ablation: the DECAAF study. *JAMA* 2014;**311**:498–506.
9. Cochet H, Mouries A, Nivet H, Sacher F, Derval N, Denis A, Merle M, Relan J, Hocini M, Haissaguerre M, Laurent F, Montaudon M, Jais P. Age, atrial fibrillation, and structural heart disease are the main determinants of left atrial fibrosis detected by delayed-enhanced magnetic resonance imaging in a general cardiology population. *J Cardiovasc Electrophysiol* 2015;**26**:484–492.
10. Spach MS, Dolber PC, Heidlage JF. Interaction of inhomogeneities of repolarization with anisotropic propagation in dog atria. A mechanism for both preventing and initiating reentry. *Circ Res* 1989;**65**:1612–1631.
11. Tanaka K, Zlochiver S, Vikstrom KL, Yamazaki M, Moreno J, Klos M, Zaitsev AV, Vaidyanathan R, Auerbach DS, Landas S, Guiraudon G, Jalife J, Berenfeld O, Kalifa J. Spatial distribution of fibrosis governs fibrillation wave dynamics in the posterior left atrium during heart failure. *Circ Res* 2007;**101**:839–847.
12. Li D, Fareh S, Leung TK, Nattel S. Promotion of atrial fibrillation by heart failure in dogs: atrial remodeling of a different sort. *Circulation* 1999;**100**:87–95.
13. Burstein B, Comtois P, Michael G, Nishida K, Villeneuve L, Yeh YH, Nattel S. Changes in connexin expression and the atrial fibrillation substrate in congestive heart failure. *Circ Res* 2009;**105**:1213–1222.
14. Verheule S, Sato T, Everett T, Engle SK, Otten D, Rubart-von der Lohe M, Nakajima HO, Nakajima H, Field LJ, Olgin JE. Increased vulnerability to atrial fibrillation in transgenic mice with selective atrial fibrosis caused by overexpression of TGF-beta1. *Circ Res* 2004;**94**:1458–1465.
15. Hansen BJ, Zhao J, Csepe TA, Moore BT, Li N, Jayne LA, Kalyanasundaram A, Lim P, Bratasz A, Powell KA, Simonetti OP, Higgins RS, Kilic A, Mohler PJ, Janssen PM, Weiss R, Hummel JD, Fedorov VV. Atrial fibrillation driven by micro-anatomic intramural re-entry revealed by simultaneous sub-epicardial and sub-endocardial optical mapping in explanted human hearts. *Eur Heart J* 2015;**36**:2390–2401.
16. Jadidi AS, Cochet H, Shah AJ, Kim SJ, Duncan E, Miyazaki S, Sermesant M, Lehrmann H, Lederlin M, Linton N, Forclaz A, Nault I, Rivard L, Wright M, Liu X, Scherr D, Wilton SB, Roten L, Pascale P, Derval N, Sacher F, Knecht S, Keyl C, Hocini M, Montaudon M, Laurent F, Haissaguerre M, Jais P. Inverse relationship between fractionated electrograms and atrial fibrosis in persistent atrial fibrillation: combined magnetic resonance imaging and high-density mapping. *J Am Coll Cardiol* 2013;**62**:802–812.
17. Raya SP, Udupa JK. Shape-based interpolation of multidimensional objects. *IEEE Trans Med Imaging* 1990;**9**:32–42.
18. Prassl AJ, Kickinger F, Ahammer H, Grau V, Schneider JE, Hofer E, Vigmond EJ, Trayanova NA, Plank G. Automatically generated, anatomically accurate meshes for cardiac electrophysiology problems. *IEEE Trans Biomed Eng* 2009;**56**:1318–1330.
19. Krueger M, Schmidt V, Tobón C, Weber F, Lorenz C, Keller DJ, Barschdorf H, Burdumy M, Neher P, Plank G, RhodeK, Seemann G, Sanchez-Quintana D, Saiz J, Razavi R, Dössel O. Modeling atrial fiber orientation in patient-specific geometries: a semi-automatic rule-based approach. In Metaxas D, Axel L (eds). *Functional Imaging and Modeling of the Heart*. Berlin: Springer, 2011. pp. 223–232.
20. McDowell KS, Vadakkumpadan F, Blake R, Blauer J, Plank G, MacLeod RS, Trayanova NA. Methodology for patient-specific modeling of atrial fibrosis as a substrate for atrial fibrillation. *J Electrocardiol* 2012;**45**:640–645.
21. McDowell KS, Vadakkumpadan F, Blake R, Blauer J, Plank G, Macleod RS, Trayanova NA. Mechanistic inquiry into the role of tissue remodeling in fibrotic lesions in human atrial fibrillation. *Biophys J* 2013;**104**:2764–2773.
22. McDowell KS, Zahid S, Vadakkumpadan F, Blauer J, MacLeod RS, Trayanova NA. Virtual electrophysiological study of atrial fibrillation in fibrotic remodeling. *PLoS One* 2015;**10**: e0117110.
23. Courtemanche M, Ramirez RJ, Nattel S. Ionic mechanisms underlying human atrial action potential properties: insights from a mathematical model. *Am J Physiol* 1998;**275**: H301–H321.
24. Krummen DE, Bayer JD, Ho J, Ho G, Smetak MR, Clopton P, Trayanova NA, Narayan SM. Mechanisms of human atrial fibrillation initiation: clinical and computational studies of repolarization restitution and activation latency. *Circ Arrhythm Electrophysiol* 2012;**5**:1149–1159.
25. Konings KT, Kirchhof CJ, Smeets JR, Wellens HJ, Penn OC, Allessie MA. High-density mapping of electrically induced atrial fibrillation in humans. *Circulation* 1994;**89**: 1665–1680.
26. Nattel S, Burstein B, Dobrev D. Atrial remodeling and atrial fibrillation: mechanisms and implications. *Circ Arrhythm Electrophysiol* 2008;**1**:62–73.
27. Corradi D, Callegari S, Maestri R, Benussi S, Alfieri O. Structural remodeling in atrial fibrillation. *Nat Clin Pract Cardiovasc Med* 2008;**5**:782–796.
28. Kakkar R, Lee RT. Intramyocardial fibroblast myocyte communication. *Circ Res* 2010; **106**:47–57.
29. Avila G, Medina IM, Jimenez E, Elizondo G, Aguilar CI. Transforming growth factor-beta1 decreases cardiac muscle L-type Ca2+ current and charge movement by acting on the Cav1.2 mRNA. *Am J Physiol Heart Circ Physiol* 2007;**292**:H622–H631.
30. Ramos-Mondragon R, Vega AV, Avila G. Long-term modulation of Na+ and K+ channels by TGF-beta1 in neonatal rat cardiac myocytes. *Pflugers Arch* 2011;**461**:235–247.
31. Pedrotty DM, Klinger RY, Kirkton RD, Bursac N. Cardiac fibroblast paracrine factors alter impulse conduction and ion channel expression of neonatal rat cardiomyocytes. *Cardiovasc Res* 2009;**83**:688–697.
32. Vigmond EJ, Aguel F, Trayanova NA. Computational techniques for solving the bidomain equations in three dimensions. *IEEE Trans Biomed Eng* 2002;**49**:1260–1269.
33. Vigmond EJ, Hughes M, Plank G, Leon LJ. Computational tools for modeling electrical activity in cardiac tissue. *J Electrocardiol* 2003;**36** Suppl:69–74.
34. Narayan SM, Krummen DE, Rappel WJ. Clinical mapping approach to diagnose electrical rotors and focal impulse sources for human atrial fibrillation. *J Cardiovasc Electrophysiol* 2012;**23**:447–454.
35. Eason J, Trayanova N. Phase singularities and termination of spiral wave reentry. *J Cardiovasc Electrophysiol* 2002;**13**:672–679.
36. Kriegel H-P, Kröger P, Sander J, Zimek A. Density-based clustering. *WIRES Data Mining Knowl Discov* 2011;**1**:231–240.
37. Boyle PM, Veenhuyzen GD, Vigmond EJ. Fusion during entrainment of orthodromic reciprocating tachycardia is enhanced for basal pacing sites but diminished when pacing near Purkinje system end points. *Heart Rhythm* 2013;**10**:444–451.
38. Oster HS, Taccardi B, Lux RL, Ershler PR, Rudy Y. Noninvasive electrocardiographic imaging: reconstruction of epicardial potentials, electrograms, and isochrones and localization of single and multiple electrocardiac events. *Circulation* 1997;**96**:1012–1024.
39. Haissaguerre M, Hocini M, Shah AJ, Derval N, Sacher F, Jais P, Dubois R. Noninvasive panoramic mapping of human atrial fibrillation mechanisms: a feasibility report. *J Cardiovasc Electrophysiol* 2013;**24**:711–717.
40. Cochet H, Dubois R, Relan J, Zahid S, Aljefairi N, Yamashita S, Sellal J, Berte B, Amraoui S, Denis A, Derval N, Boyle P, Trayanova N, Sacher F, Hocini M, Jais P. Relationship between rotor activity and fibrosis in persistent atrial fibrillation: a combined noninvasive mapping and MRI study. *Heart Rhythm* 2015;**12**:S512.
41. Cochet H, Dubois R, Relan J, Zahid S, Aljefairi N, Yamashita S, Sellal J, Berte B, Amraoui S, Denis A, Derval N, Boyle P, Trayanova N, Sacher F, Hocini M, Jais P. Relationship between rotor activity and fibrosis in persistent atrial fibrillation: a combined noninvasive mapping and MRI study. *Heart Rhythm* 2015;**12**:S512.
42. de Groot NM, Houben RP, Smeets JL, Boersma E, Schotten U, Schalij MJ, Crijns H, Allessie MA. Electropathological substrate of longstanding persistent atrial fibrillation in patients with structural heart disease: epicardial breakthrough. *Circulation* 2010; **122**:1674–1682.
43. Bollmann A, Sonne K, Esperer HD, Toepffer I, Langberg JJ, Klein HU. Non-invasive assessment of fibrillatory activity in patients with paroxysmal and persistent atrial fibrillation using the Holter ECG. *Cardiovasc Res* 1999;**44**:60–66.
44. Pandit SV, Jalife J. Rotors and the dynamics of cardiac fibrillation. *Circ Res* 2013;**112**: 849–862.
45. Shajahan TK, Sinha S, Pandit R. Spiral-wave dynamics depend sensitively on inhomogeneities in mathematical models of ventricular tissue. *Phys Rev E Stat Nonlin Soft Matter Phys* 2007;**75**:011929.
46. Defauw A, Dawyndt P, Panfilov AV. Initiation and dynamics of a spiral wave around an ionic heterogeneity in a model for human cardiac tissue. *Phys Rev E Stat Nonlin Soft Matter Phys* 2013;**88**:062703.
47. Hocini M, Sanders P, Jais P, Hsu LF, Takahashi Y, Rotter M, Clementy J, Haissaguerre M. Techniques for curative treatment of atrial fibrillation. *J Cardiovasc Electrophysiol* 2004; **15**:1467–1471.
48. Zhu D, Wu Z, van der Geest RJ, Luo Y, Sun J, Jiang J, Chen Y. Accuracy of late gadolinium enhancement - magnetic resonance imaging in the measurement of left atrial substrate remodeling in patients with rheumatic mitral valve disease and persistent atrial fibrillation. *Int Heart J* 2015;**56**:505–510.
49. Karamitsos TD, Neubauer S. Detecting diffuse myocardial fibrosis with CMR: the future has only just begun. *J Am Coll Cardiol Img* 2013;**6**:684–686.
50. Monnerat-Cahli G, Alonso H, Gallego M, Alarcon ML, Bassani RA, Casis O, Medei E. Toll-like receptor 4 activation promotes cardiac arrhythmias by decreasing the transient outward potassium current (Ito) through an IRF3-dependent and MyD88-independent pathway. *J Mol Cell Cardiol* 2014;**76**:116–125.
51. Yue L, Feng J, Gaspo R, Li GR, Wang Z, Nattel S. Ionic remodeling underlying action potential changes in a canine model of atrial fibrillation. *Circ Res* 1997;**81**:512–525.
52. Costa CM, Campos FO, Prassl AJ, dos Santos RW, Sanchez-Quintana D, Ahammer H, Hofer E, Plank G. An efficient finite element approach for modeling fibrotic clefts in the heart. *IEEE Trans Biomed Eng* 2014;**61**:900–910.
53. Wolf RM, Glynn P, Hashemi S, Zarei K, Mitchell CC, Anderson ME, Mohler PJ, Hund TJ. Atrial fibrillation and sinus node dysfunction in human ankyrin-B syndrome: a computational analysis. *Am J Physiol Heart Circ Physiol* 2013;**304**:H1253–H1266.